ChemSusChem
Research Article
doi.org/10.1002/cssc.202402779
Chemistry Europe
European Chemical Societies Publishing

www.chemsuschem.org

Air-Stable High-Voltage Li-Ion Organic Cathode Enabled by Localized High-Concentration Electrolyte

Alae Eddine Lakraychi,* Ifeanyi Emmanuel Udom, Wen Ren, and Yan Yao*

While lithium-ion batteries have revolutionized the field of energy storage, their reliance on critical minerals such as cobalt and nickel raises significant concerns over resource availability and supply chain uncertainty. In this study, we revisit dithiin-fused dilithium naphthazarin (5,8-dihydroxy-1,4-naphthoquinone) (DNP-Li) as a high-voltage Li-ion organic cathode and evaluate its performance in conjunction with localized high-concentration electrolyte (LHCE). DNP-Li exhibits remarkable air and thermal stability, a high operating potential of 3.55 V vs. Li^+/Li, and a specific capacity of 232 mAh g^{-1}, positioning it as one of the most promising candidates among Li-ion organic cathodes. Furthermore, the electrochemical behavior of DNP-Li is strongly influenced by the electrolyte composition, giving distinct two-plateau or four-plateau voltage profiles accompanied by reversible or irreversible phase transitions in carbonate-based or LHCE electrolyte formulations, respectively. The reduced solubility of DNP-Li-based redox intermediates in LHCE enhances cycling stability, achieving a capacity retention of 85% after 50 cycles at 0.1C and 75% after 160 cycles at 0.5C, demonstrating a significant improvement compared to the carbonate-based electrolyte. This work highlights the critical role of solute–electrolyte interactions in modulating the electrochemical performance of multielectron small-molecule organic cathodes, offering new pathways for advancing sustainable and high-efficiency energy storage technologies.

1. Introduction

Li-ion batteries (LIBs) have profoundly transformed our modern society, dominating portable electronic devices for over three decades.[1] Today, with the global adoption of electric vehicles, LIBs are foreseen to make a greater impact by enabling the transition from fossil fuels to renewable energies.[2,3] This increasing reliance on LIBs has led to a surge in demand, raising critical concerns regarding the availability and supply of raw materials, as well as the management of their life cycle.[4,5]

The cathode material represents about 50% of the battery cost and is predominantly composed of critical commodity elements such as cobalt (Co) and nickel (Ni).[6] Notably, the majority of global Co production is derived from mining operations in the Democratic Republic of Congo (DRC),[7] while refining and processing are primarily concentrated in China.[4] This reliance on geographically concentrated resources is expected to introduce significant sociopolitical risks and expose the market to unpredictable price volatility.

To promote sustainability, diversification of battery chemistries utilizing abundant and geographically diverse raw materials is regarded as a promising strategy that could complement LIBs in achieving global clean energy goals.[1,8–11] Organic batteries are emerging as a credible alternative, offering advantages such as high theoretical capacities, mild synthetic conditions, and ease of recyclability.[12–14] A comparable Li-ion cell configuration can be realized by the integration of a Li-reservoir organic cathode. However, the development of such cathodes remains in its nascent stages, with the chemical space currently restricted to a limited number of reported examples exhibiting low operating potentials.[15–18]

Recently, Yao and colleagues reported a novel organic cathode based on dithiin-fused dilithium naphthazarin (5,8-dihydroxy-1,4-naphthoquinone), designated as DNP-Li.[19] This multielectron organic molecule incorporates both carbonyl and dithiin redox sites.[20,21] Theoretically, this molecule can exchange up to 10 electrons per molecule: 8 electrons through cation (Li^+) uptake at the carbonyl sites (n-type) and 2 electrons via anion uptake at the dithiin ring (*p*-type), giving a theoretical capacity of 570 mAh g^{-1} (Figure S1, Supporting Information and associated notes). In practice, anion uptake was found to be irreversible, with only Li^+ exhibiting reversible behavior over a wide potential range of 4.0–1.5 V vs. Li^+/Li, resulting in a practically exploitable capacity of 464 mAh g^{-1}. Despite these promising features, the large operating potential window poses challenges to the applicability of DNP-Li as either cathode or anode material.

Since the pristine state of DNP-Li corresponds to a lithium-containing, half-discharged state (i.e., state of charge (SoC) of 50%), the compound could be utilized in the high potential range (>3.0 V vs. Li^+/Li), where the electrochemical process

---

A. E. Lakraychi, I. E. Udom, Y. Yao
Department of Electrical and Computer Engineering
University of Houston
Houston, TX 77204, USA
E-mail: alakrayc@central.uh.edu
yyao4@central.uh.edu

A. E. Lakraychi, Y. Yao
Texas Center for Superconductivity at the University of Houston (TcSUH)
University of Houston
Houston, TX 77204, USA

W. Ren
Department of Chemical and Biomolecular Engineering
University of Houston
Houston, TX 77204, USA

Supporting information for this article is available on the WWW under https://doi.org/10.1002/cssc.202402779

begins with Li^+ extraction, thereby serving as a high-voltage Li-ion organic cathode with a competitive specific capacity of 232 mAh g^{-1}, corresponding to the exchange of 4 electrons per molecule (**Figure 1**a).

Herein, we investigated DNP-Li as an air-stable, high-voltage Li-ion organic cathode in conjunction with localized high-concentration electrolyte (LHCE) for LIBs. DNP-Li demonstrated high thermal stability up to 450 °C and resistance to air oxidation for up to 4 months, with only water adsorption, which can be effectively removed by low-temperature vacuum drying. A comparative study of the electrochemical and physicochemical properties of DNP-Li in both carbonate-based and LHCE electrolyte formulations revealed that its redox reaction pathway is highly dependent on the electrolyte composition. Specifically, a reversible phase transition was observed in the carbonate-based electrolyte, whereas an irreversible phase transition occurred in LHCE. Furthermore, the significantly reduced dissolution of DNP-Li-based redox intermediates in LHCE resulted in enhanced cycling stability, achieving a capacity retention of 85% after 50 cycles at 0.1C.

2. Results and Discussion

2.1. DNP-Li as a High-Voltage Li-Ion Organic Cathode

The electrochemical storage properties of DNP-Li were evaluated galvanostatically within the 4.0–2.8 V vs. Li^+/Li potential range at a cycling rate of 0.1C (where 1C corresponds to a full charge in 1 h) (Figure 1b). The resulting galvanostatic voltage profile reveals a reversible electrochemical extraction/uptake of Li^+ process, characterized by two pseudo-plateaus during the charge, delivering the theoretical capacity. This is followed by two distinct, equal-capacity plateaus during the discharge, yielding a specific capacity of 205 mAh g^{-1} and an initial coulombic efficiency (ICE) of 90%. In the 2nd cycle, the voltage profile traces back the discharge profile with minimum polarization, delivering a specific capacity of 194 mAh g^{-1} at an average operating potential of 3.55 V vs. Li^+/Li, representing one of the highest operating potentials reported for Li-ion organic cathodes (Figure 1c).[16–18,22–29] These exceptional material-level energy metrics position DNP-Li within the performance range of inorganic Li-ion cathodes, exceeding the capability of $LiFePO_4$ (Figure 1d).[30] $LiFePO_4$ was selected for comparison due to its superior sustainability compared to other state-of-the-art Li-ion cathode materials. However, DNP-Li exhibits significant capacity fade (Figure S2, Supporting Information), attributed to changes in the physicochemical properties of its intermediate states at different SoCs, as detailed below.

The outstanding high operating potential of DNP-Li is highly unusual for a simple unsubstituted quinonoid structure.[21,31] The underlying origin of such a potential increase was not addressed in Yao's work and remains unexplained. Based on our analysis of the molecular structure-operating voltage relationship of organic cathodes available in the literature, we hypothesize that this increased voltage arises from a significant reduction in the electron density of the organic molecule, attributed to the presence of adjacent carbonyl groups acting as electron-withdrawing substituents (Figure S3 and S4, Supporting Information and associated notes).[18,32] For instance, the charging potential of dilithium (2,5-dilithium-oxy)-terephthalate salt (Li_4-p-DHT) averages 2.65 V vs. Li^+/Li.[33] However, in an equivalent redox molecule containing additional carbonyl groups, dilithium (3,6-dilithium-oxy)-2,5-dimethoxybenzoquinone (Li_2-DHDMQ), the charging potential increases to 3.0 V vs. Li^+/Li.[32] To further validate this hypothesis, we synthesized a novel non-aromatic carbonyl-containing conjugated sulfonamide (Li_4-PTtSAQ) and compared its voltage profile with that of its aromatic, carbonyl-free counterpart (Li_4-PTtSA).[25,29] The charging potential of Li_4-PTtSAQ exceeds 3.0 V vs. Li^+/Li, which is significantly higher than the 2.6 V vs. Li^+/Li observed for Li_4-PTtSA. To the best of our knowledge, this molecular approach has not been explored

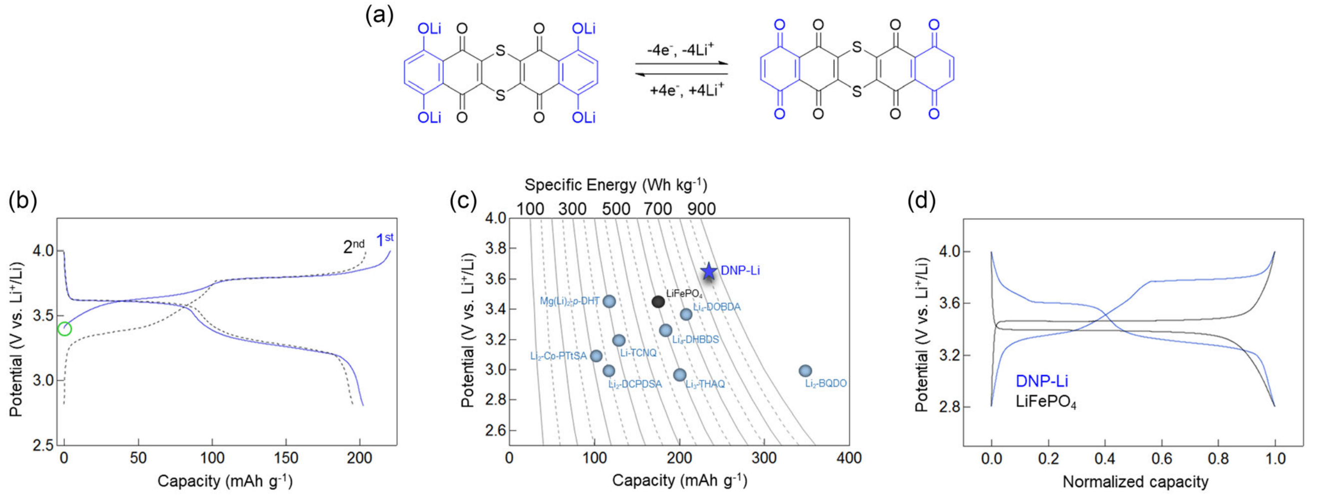

Figure 1. Electrochemical performances of DNP-Li in the high potential region. a) Schematic of the reversible four-electron redox reaction. b) Galvanostatic charge/discharge curves for two initial cycles obtained at 0.1C in LP30. The green circle indicates the starting open circuit potential. c) Comparative theoretical material-level energy metrics of DNP-Li and other air-stable Li-ion organic cathodes. d) Comparative 2nd cycle galvanostatic charge/discharge curves of DNP-Li and $LiFePO_4$.

to understand the potential tuning of Li-ion organic cathodes and will be the subject of future investigation.

2.2. Air Stability and Thermal Behavior

Beyond the characteristics of high voltage and Li-reservoir, air stability and thermal stability are key factors in the development of Li-ion cathode materials. Air stability is crucial for facilitating storage, handling, and cell manufacturing,[34] while thermal stability is vital for ensuring battery safety, as it helps prevent thermal runaway events, which are commonly observed in layered oxide cathodes.[35] To investigate the air stability of DNP-Li, the corresponding powders were analyzed by Fourier-transform infrared spectroscopy (FTIR) and powder X-ray diffraction (PXRD) following 1 week of exposure to ambient air. Thermal behavior was further examined using in situ high-temperature PXRD.

As depicted in **Figure 2**a,b, both pristine and air-exposed samples exhibit identical features. Analysis of the FTIR spectra reveals that DNP-Li exhibits excellent resistance to self-oxidation in the presence of O_2, as evidenced by the absence of carbonyl vibration bands above 1600 cm^{-1}. Similarly, it resists hydrolysis in the presence of moisture, as reflected by the absence of phenolic O—H vibration band at 3400 cm^{-1}, with the only notable change being the surface absorption of water, which can be effectively removed through thermal treatment at 100 °C. The PXRD analysis further corroborates the air stability, as all the characteristic peak positions remain unchanged, indicating that the crystal structure is well preserved. To assess long-term air stability, DNP-Li powders were exposed to ambient conditions for 4 months, with no significant changes observed in the characteristic FTIR bands or PXRD peak positions, apart from notable water uptake (Figure S5, Supporting Information). This suggests that the molecular structure and crystallinity remain intact, and the adsorbed water can be effectively removed by vacuum thermal treatment. Thermal analysis performed under argon (Figure 2c) indicates that the sample possesses excellent thermal stability up to 450 °C, beyond which two successive weight loss events are observed. This thermal behavior is further elucidated through temperature-resolved PXRD collected from 30 to 600 °C under nitrogen at a heating rate of 0.5 °C min^{-1} (Figure 2d). The results reveal that the sample preserves its crystal structure until 450 °C

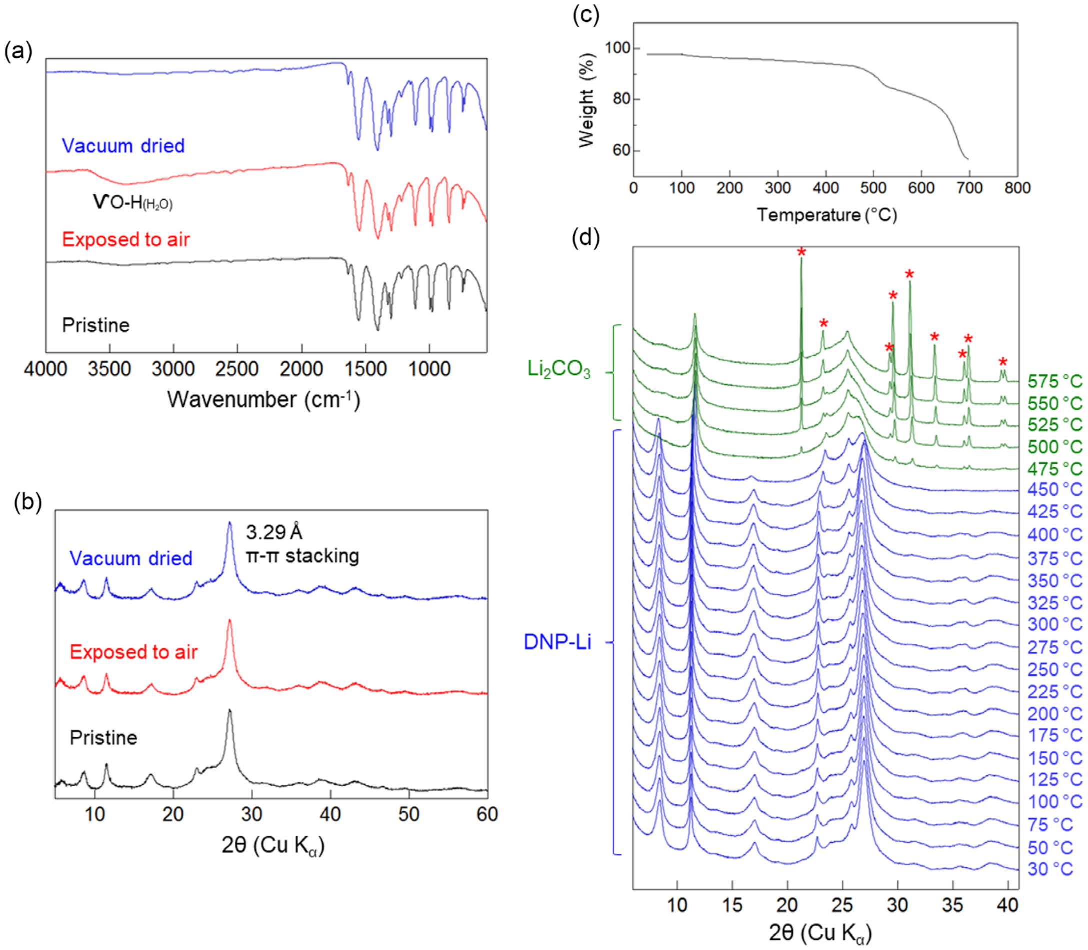

Figure 2. Air stability and thermal behavior of DNP-Li powder. a) FTIR and b) XRD survey upon exposure to ambient air for one week. Traces of adsorbed H_2O remain trapped and can be effectively removed through vacuum annealing at 100 °C. c) Thermal analysis (TG) recorded under argon at a heating rate of 5 °C min^{-1}. d) Time-resolved X-ray powder diffraction (TRXRPD) patterns collected by heating the sample under nitrogen from 30 to 575 °C at a heating rate of 0.5 °C min^{-1}. *corresponds to Li_2CO_3 diffraction peaks.

without any discernible phase transitions, in contrast to the behavior observed for dilithium (3-hydroxy-2-lithium-oxy) terephthalate (Li_2(Li,H)-o-DHT) where new phases were formed upon heating.[26] Further heating the sample above 450 °C results in decomposition, leading to the formation of crystalline lithium carbonate along with amorphous carbon as expected in the pyrolysis process. Such decomposition behavior presents a potential advantage for cost-effective and energy-efficient recyclability at the end of the material's lifecycle.[36]

2.3. Electrolyte-Dependent Reaction Pathways of DNP-Li

Similar to most small-molecule organic cathodes, the electrochemical performance of DNP-Li is dependent on the choice of electrolytes, primarily due to the potential dissolution of active material particles. Previous studies on lithium–sulfur (Li-S) batteries have highlighted the benefits of using LHCEs in reducing the solubility of lithium polysulfides, thereby enhancing cycling stability.[37–39] Inspired by these findings, we sought to address the capacity fade of DNP-Li by employing an LHCE formulation with lithium bis(fluorosulfonyl)imide (LiFSI) in dimethoxyethane (DME) and bis(2,2,2-trifluoroethyl) ether (BTFE) in a molar ratio of 0.9:1:2. For comparative purposes, the electrochemical performance of DNP-Li was investigated in both carbonate (LP30) and LHCE electrolytes, and the evolution of its physicochemical properties at various SoCs was systematically analyzed using ex situ ultraviolet–visible (UV–Vis) spectroscopy, XRD, and scanning electron microscopy (SEM) (**Figure 3** and S6, Supporting Information). The ex situ measurements were performed on isolated electrodes at distinct SoCs during the first cycle: pristine (black, 1), half-charged (orange, 2), fully charged (red, 3), and fully discharged (blue, 4).

The galvanostatic voltage profile of DNP-Li cycled in LHCE is shown in Figure 3a. During the initial charge, the voltage profile closely resembles that obtained in LP30, albeit with a slight decrease in capacity (Figure S7, Supporting Information). However, upon subsequent discharge, DNP-Li exhibits a distinct voltage profile in LHCE compared to LP30 (Figure 3a and S6a, Supporting Information). Apart from the difference in specific capacity, the most notable variation is the number of voltage

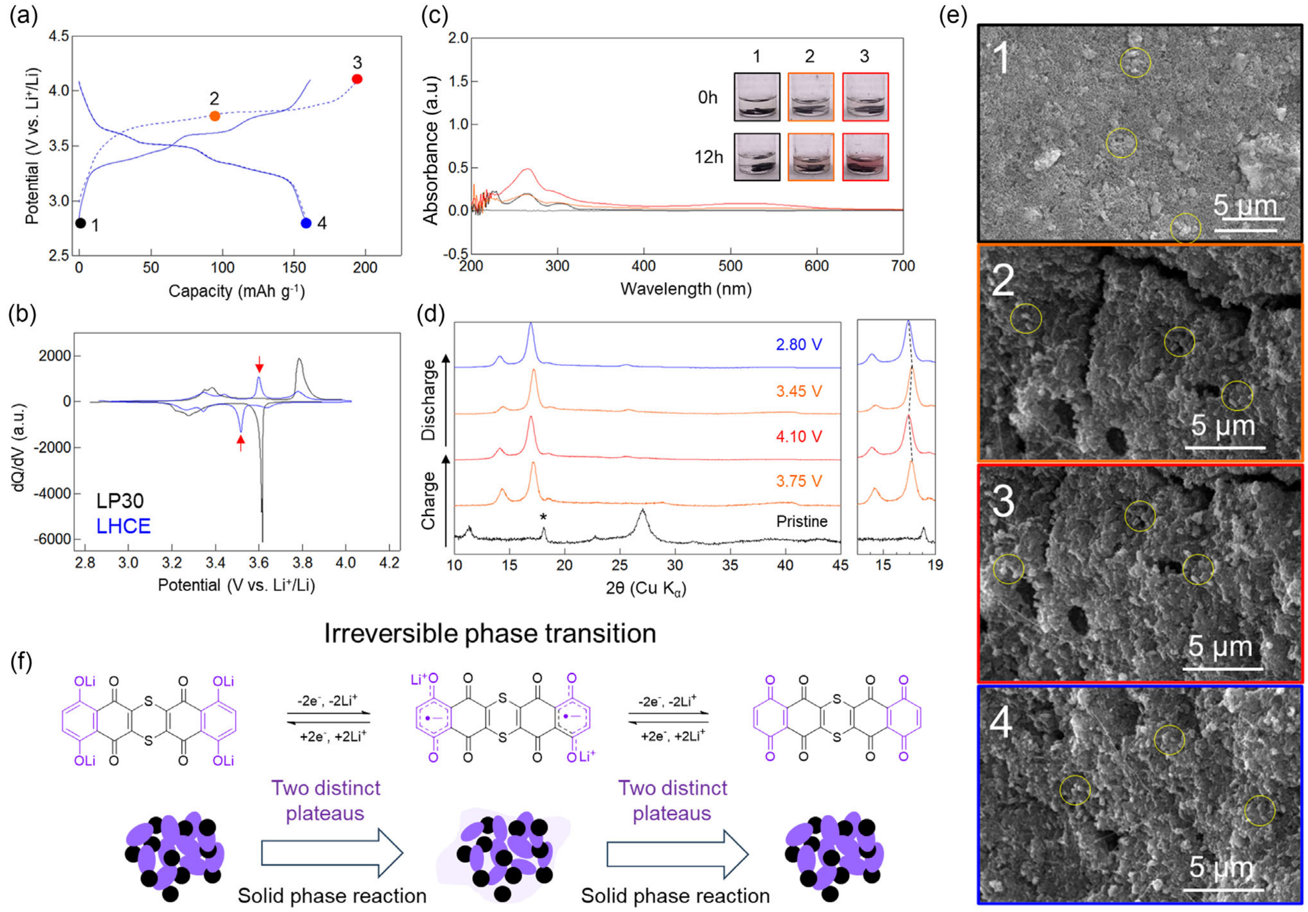

Figure 3. Reaction pathway of DNP-Li in LHCE. a) Galvanostatic charge/discharge curves for two initial cycles obtained at 0.1C in LHCE and b) corresponding 2nd cycle differential capacity vs. potential curve compared to the one from LP30. The colored dots indicate SoC or discharge at which the ex situ samples were extracted, whereas the red arrows indicate the emergence of new redox peaks. c) Ex situ UV–Vis absorption spectra (the insets are corresponding optical photographs of electrodes soaked in electrolyte showing the dissolution behaviors). d) Ex situ XRD patterns accompanied with a zoom-in focused within 12°–19° region. * corresponds to PTFE diffraction peaks. e) SEM images of pristine and cycled DNP-Li-based electrodes at various SoCs. The color codes and numbers black (1), orange (2), red (3), blue (4) indicate the pristine, half-charged, fully charged, and fully discharged states, respectively. The yellow circles highlight active material particles. All ex situ characterizations are conducted on electrodes taken from the first cycle. f) Schematic illustration of the solid-solid reaction pathway of DNP-Li in LHCE.

plateaus. In LHCE, the voltage profile comprises four short pseudo-plateaus of equal capacity, aligning with the predictions for crystalline DNP-Li as reported by Tateyama et al.[40] but contrasts with the two long flat plateaus observed in LP30. This voltage profile difference persists upon the second cycle, and it is more distinctly observed in the corresponding dQ/dV vs. potential curve, where additional redox peaks and a notable reduction in peak intensity are evident in LHCE (Figure 3b).

This finding suggests that DNP-Li may undergo different reaction pathways depending on the electrolyte composition. Specifically, a two two-electron overall process occurs in LP30, while a four one-electron overall process takes place in LHCE. Notably, similar electrochemical features have been observed for other four-electron organic cathodes, namely bis-tetraaminobenzoquinone (TAQ) and pyrene-4,5,9,10-tetraone (PTO).[41–43] TAQ exhibited a voltage profile comprising four short plateaus, likely due to its insolubility in the electrolyte, whereas PTO demonstrated two long plateaus, attributed to its known dissolution in electrolytes. This suggests that the voltage profile difference for DNP-Li may be attributed to its reduced dissolution in LHCE.

To further investigate the solubility behavior of DNP-Li, its saturation solubility in LP30 and LHCE was quantified using UV–Vis titration (Figure S8a–c, Supporting Information and associated notes for experimental details). The measured solubility was found to be higher in LP30 (1.51 mM) compared to LHCE (0.32 mM). However, the solubility of DNP-Li in LP30 remains insufficient to induce significant dissolution, suggesting that charged intermediate species exhibit greater solubility. Due to the challenges associated with the chemical synthesis of delithiated DNP-Li, a quantitative solubility determination could not be performed. Instead, assuming a similar molar absorption coefficient for DNP-Li intermediates, a qualitative solubility assessment was conducted by measuring the UV–Vis absorption of DNP-Li electrodes at 0%, 50%, and 100% SoCs.

In LHCE (Figure 3c), a colorless solution was observed for the pristine (1) electrode, while progressively more coloration appeared for the half-charged (2) and fully charged (3) electrodes. This trend is consistent with the corresponding absorbance in UV–Vis absorption spectra. Conversely, in LP30 (Figure S6b, Supporting Information), colored electrolyte solutions were observed for pristine (1), half-charged (2), and fully charged (3) electrodes, indicating dissolution of DNP-Li across all SoCs. The corresponding UV–Vis spectra reveal varying degrees of absorption, suggesting differing solubility, following the trend: half-charged (orange) > fully charged (red) > pristine (black). Furthermore, the highest absorbance of DNP-Li in LP30 is ≈1.6 for the half-charged state, nearly ten times greater than the corresponding absorbance observed in LHCE, demonstrating that the dissolution of DNP-Li redox species is significantly reduced in LHCE.

Interestingly, ex situ XRD analysis reveals that DNP-Li undergoes different phase transitions depending on the electrolyte composition. In LHCE (Figure 3d), after the extraction of two Li^+ at 3.75 V, the peaks at 11.4° and 27.1°, present in the pristine state, disappear, giving rise to new peaks at 14.4° and 17.5°, suggesting the formation of a new phase. Further extraction of the remaining two Li^+ at 4.1 V results in no significant phase change, except for a minor shift of the peaks to lower angles. Similarly, the subsequent Li^+ uptake at 3.45 V induces a slight shift of the peaks to higher angles, followed by a minor shift to lower angles at 2.8 V, indicating an overall irreversible phase transition. Similar behavior was also recorded for Li_4-DHBDS as reported by Lakraychi et al. where an irreversible phase transition was observed during the first cycle.[23] In contrast, the extraction of the first two Li^+ at 3.75 V in LP30 (Figure S6c, Supporting Information) leads to a significant reduction in the intensity of the peaks associated with the pristine phase (phase a), accompanied by the emergence of a new phase (phase b). This new phase continues to grow after the extraction of the remaining two Li^+ at 4.1 V. A reverse phase transition is observed during the subsequent Li^+ uptake, where phase b significantly diminishes at 3.45 V, giving rise to phase a, which further grows at 2.8 V, although poorly crystalline, suggesting a seemingly reversible phase transition.

SEM images of pristine DNP-Li powders are shown in Figure S9, Supporting Information. The active material consists of submicrometric, irregularly shaped particles, which are uniformly embedded within the carbon matrix after electrode preparation (Figure 3e, image 1). In LHCE, the electrode maintains its particle integrity without any noticeable morphological changes (Figure 3e, images 2–4). These observations indicate that most of the electrochemical reaction takes place in the solid phase, thereby explaining the four-plateau electrochemical behavior. In contrast, in LP30, at the half-charged state (Figure S6, Supporting Information image 2), the original active material particles disappear, while accompanied by new submicrometric, needle-like particles precipitate. At the fully charged state (Figure S6d, Supporting Information, image 3), these particles undergo further growth, transforming into angular micrometric particles that persist and remain morphologically unchanged at the fully discharged state (Figure S6d, Supporting Information, image 4). These observations strongly suggest that DNP-Li undergoes a dissolution–precipitation reaction pathway in LP30, which could also contribute to the two-plateau electrochemical behavior.

In summary, the reaction pathway of DNP-Li is strongly dependent on the electrolyte composition. In LHCE (Figure 3f), DNP-Li maintains its solid phase throughout the redox reaction, exhibiting minimal changes in particle size and morphology, alongside an irreversible phase transition. This behavior corresponds to four distinct plateaus, likely associated with both solid-phase delithiation/lithiation as well as phase transition. In contrast, in LP30 (Figure S6e, Supporting Information), the dissolution of DNP-Li leads to substantial changes in particle size and morphology, accompanied by a reversible phase transition, yielding two distinct redox plateaus, likely attributed to the solid–liquid–solid delithiation/lithiation. A comprehensive understanding of the charge storage mechanism of DNP-Li requires further investigation, particularly into the initial, intermediate, and final crystal structures of DNP-Li involved in each reaction pathway.

2.4. Cycling Stability in LHCE

The voltage profiles of selected cycles in LHCE further confirm the consistency of the four-plateau behavior throughout cycling, suggesting that this reaction pathway is an intrinsic characteristic rather than a transient phenomenon (**Figure 4**a). Apart from the capacity loss occurring during the first discharge, only a slight capacity fade is observed. This trend is further reflected in the cycling stability, where DNP-Li retains 85% of its discharge capacity after 50 cycles at 0.1C (Figure 4b). In contrast, when cycled in LP30 under similar conditions, the compound exhibits a lower capacity retention of 67% after 30 cycles, with most of the capacity fading occurring progressively over the first 10 cycles (Figure S10a, Supporting Information). These findings suggest that the primary cause of capacity degradation in LP30 is the dissolution of DNP-Li, whereas the low ICE is the predominant factor in LHCE. Notably, the low ICE cannot be attributed to a side reaction between lithium metal and shuttled DNP-Li species (Figure S11, Supporting Information); however, the underlying mechanisms require further investigation.

The rate capability of DNP-Li was evaluated in both electrolytes. The characteristic four-plateau behavior appears to be restricted to low *C*-rates, as it transitions into two pseudo-plateaus with increasing *C*-rate (Figure 4c). This transition is accompanied by a rise in overpotential and a decrease in specific capacity, likely due to the limited Li^+ diffusion within the solid particles. A similar trend was also observed for PTO when less-dissolving electrolyte was employed.[44] However, the initial specific capacity and the four-plateau behavior were restored when decreasing the *C*-rate to 0.1C. In contrast, the rate capability appears to be less affected in LP30, as the compound demonstrates lower overpotential and reduced capacity degradation with increasing *C*-rate (Figure S10b, Supporting Information), likely attributed to the enhanced Li^+ diffusion facilitated by the liquid phase reaction.[45]

Overall, the introduction of LHCE not only minimizes DNP-Li dissolution but also intrinsically modulates its redox reaction pathway, resulting in distinct electrochemical behavior. Such modulation of electrochemical behavior has been extensively studied in Li-S batteries, where the voltage profiles and solubility of lithium polysulfides are significantly influenced by the solvation energy.[39] However, such solvation-property relationships remain underexplored in the field of organic batteries. Although organic batteries and Li-S batteries share seemingly similar working principles, they are expected to exhibit distinct behaviors due to the diverse chemical nature of organic redox species, which give rise to different solute-solvent and solute-cation interactions compared to those observed in Li-S batteries. Furthermore, DNP-Li demonstrates that competitive energy metrics could be achieved using entirely naturally abundant elements (e.g., C, H, N, O, and S), akin to TAQ, which has shown that competitive electrical conductivity could be attained from the same elements.[43] If these features can be integrated into a single organic material, it could represent a significant breakthrough

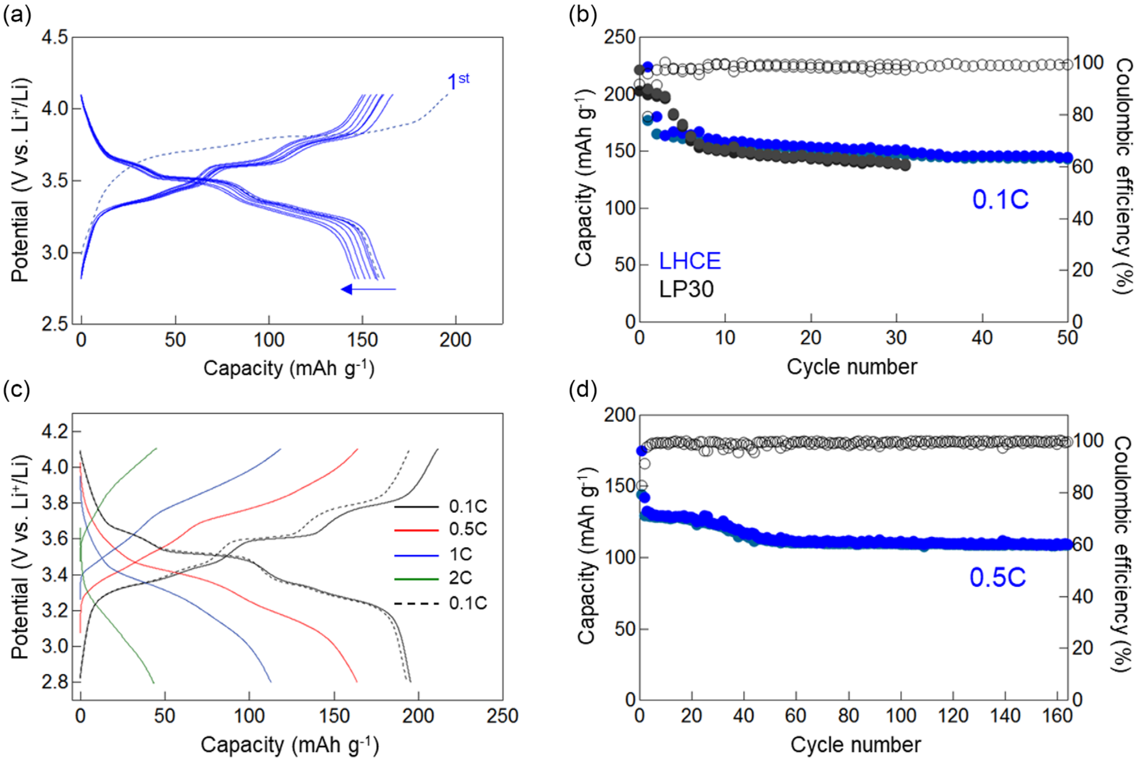

Figure 4. Cycling performance of DNP-Li in LHCE. a) Galvanostatic charge/discharge curves of DNP-Li cycled at 0.1C, highlighting the retention of the four-plateau reaction pathway over selected cycles (1st, 2nd, 5th, 10th, 15th, 20th, 25th, and 30th). b) Comparative cycling stability of DNP-Li cycled at 0.1C in LHCE and LP30. c) Galvanostatic charge/discharge curves of the DNP-Li electrode measured at different C-rates ranging from 0.1 to 2C. d) Extended cycling stability in LHCE at 0.5C.

towards the commercial viability of organic batteries. Despite certain challenges, the field of organic batteries presents a fertile chemical playground, warranting further exploration for the development of sustainable and competitive energy storage systems.

3. Conclusions

This work demonstrates the viability of DNP-Li as a high-voltage Li-ion organic cathode, offering competitive material-level energy metrics along with remarkable air and thermal stability. The employment of a conventional carbonate-based electrolyte leads to DNP-Li dissolution, resulting in two voltage plateaus alongside a reversible phase transition. In contrast, the use of LHCE significantly reduces the dissolution of DNP-Li-based redox intermediates, leading to improved cycling stability and a reaction pathway characterized by four voltage plateaus and an irreversible phase transition. This work underscores the importance of electrolyte composition in modulating the electrochemical behavior and reaction pathways of multielectron small-molecule organic cathodes, an area that remains underexplored in the field of organic batteries. Future studies should focus on optimizing electrolyte formulations and investigating solute–electrolyte interactions at different SoCs to fully exploit their potential for sustainable and high-performance organic batteries.

4. Experimental Section

Materials and Methods

DNP-Li (CAS: 1882849-59-3) was purchased from TCI Chemical. The following chemicals and solvents were purchased from Sigma-Aldrich and used as received without further purification: methanesulfonyl chloride (MsCl, 97%), tetrabutylammonium perchlorate (TBAP, 99%), lithium hydride (LiH, 95%), pyridine (99%), isopropanol (99.9%, HPLC grade), anhydrous dimethylformamide (DMF, 99.8%), anhydrous tetrahydrofuran (THF, 99.8%), anhydrous dimethyl carbonate (DMC, 99%), anhydrous dimethoxyethane (DME, 99.5%), and 60 wt% polytetrafluoroethylene (PTFE) dispersion. Carbon super P was purchased from MTI, bis(fluorosulfonyl)imide lithium salt (LiFSI, 99.9%) was provided by Solvionic, 1M $LiPF_6$ in EC/DMC (LP30) was purchased from Gotion, and anhydrous bis(2,2,2-trifluoroethyl) ether (BTFE, 99%) was provided by Synguest.

Attenuated total reflectance-Fourier-transform infrared spectra were recorded on a Thermo Scientific Nicolet iS5 spectrometer. The relative humidity is about 30–40%. UV–Vis spectra were recorded on an Agilent Cary 60 spectrometer between 800 and 200 nm wavelengths. Thermogravimetric analysis (TGA) was carried out under argon with a SENSYSevo instrument from Setaram using a heating rate of 5 °C min^{-1} between room temperature and 700 °C. Scanning electron microscope (SEM) measurements were conducted using an FEI XL-30 FEG at 5 kV. Before SEM analysis, the samples were sputtered with a 3 nm gold layer to avoid charge accumulation.

PXRD

Patterns were recorded in reflection mode (Bragg–Bentano geometry) using Rigaku MiniFlex 600 with Cu Kα radiation ($\lambda = 1.5406$ Å) operating at 40 kV–15 mA. The data were recorded in 2θ range of 5°–60° with a step width of 0.01° and a scan rate of 1.8° min^{-1}. Temperature-resolved PXRD (TRPXRD) measurements were performed in a 1.4 mm-diameter polyimide capillary in transmission mode (Debye–Scherrer geometry) using a Rigaku Smart Lab diffractometer equipped with a $\theta/2\theta$ reflection geometry and PhotonMax high-flux 9 kW rotating anode X-ray source using Cu Kα radiation ($K\alpha_1 = 1.5406$ Å, $K\alpha_2 = 1.5444$ Å, $K\alpha_2/K\alpha_1 = 0.5$). The tube voltage and current were 45 kV and 200 mA, respectively. The data were recorded in 2θ range of 5°–45° with a step width of 0.01° and a scan rate of 1° min^{-1}. Ex situ XRD measurements were performed on DNP-Li electrodes using the electrode composition as detailed in the subsequent section.

UV–Vis Sample Preparation

Pristine and cycled electrodes were soaked in 200 μL of electrolyte for 3 days. Afterwards, 100 μL of each solution was diluted in 3 mL of DME to measure the absorbance using UV–Vis spectroscopy.

Electrochemistry

Cyclic voltammetry was performed with a Biologic Science Instrument VMP3. A three-electrode cell setup with a glassy carbon working electrode (3 mm diameter, CH instruments), a platinum wire counter electrode (CH instruments), a silver wire pseudo-reference electrode, and a supporting electrolyte consisting of 0.1 M TBAP in anhydrous DMF were used for measurements. Typically, 1 mM of active material was dissolved in the electrolyte solution. The voltammograms were recorded inside a glovebox at a scan rate of 100 mV s^{-1} and at room temperature. Ferrocene was added to the solution after testing and used as an internal reference.

Cell Preparation and Electrochemical Measurements

All experiments were performed at room temperature, and all cells were assembled in an mBRAUN argon-filled glovebox (<0.5 ppm water and oxygen content). Electrochemical measurements were recorded on a Bio-Logic VMP3 potentiostat. Active material, Csp, and PTFE binder were mixed in a 5:4:1 mass ratio in an agate mortar for 20 min. Isopropanol (1.5 $mL_{isopropanol}\, g_{paste}^{-1}$) was used to improve mixing and malleability. The resulting rubber-like composite was calendared, dried in air for 6 h, and then dried under vacuum at 70 °C overnight. Afterwards, the self-standing electrode was cut into discs of diameter 5/16 inch. The typical areal mass loading of these composite electrodes is 2 mg cm^{-2}. Swagelok cells were assembled using lithium foil with a 3/8 inch diameter, a glass fiber separator (Whatman, Grade GF/A, 7/16 inch) impregnated with 70 μL of electrolyte, and the above-prepared electrodes as cathodes. The cells were cycled inside the glovebox within different potential windows at a cycling rate of 0.1C.

Computational Details

DFT calculations were performed using the Gaussian16 package.[46] The geometries were fully optimized in the gas phase using the Lee–Yang–Parr gradient-corrected correlation functional (B3LYP) method, and frequency calculations were performed at the same theoretical level to confirm the absence of imaginary frequencies. The lowest unoccupied molecular orbital (LUMO) analysis was performed based on the values calculated with Gaussian16.

Synthesis of Tetralithium 1,2,4,5-Tetrayltetrakis((Methylsulfonyl)Amide)Benzoquinone (Li_4-PTtSAQ)

Li_4-PTtSAQ was synthesized in a two-step synthesis starting from tetraaminobenzoquinone (TABQ). The preparation of TABQ was reproduced from the reported method,[47] whereas the synthesis of H_4-PTtSAQ was adapted from the reported method.[25] To a solution of TABQ (1.5 g, 8.9 mmol) in 30 mL pyridine, MsCl (2.9 mL, 38 mmol) was added dropwise at 0 °C. The solution was left to warm up slowly to room temperature and was kept stirring for another 24 h. After that, 100 mL of 1 M HCl solution was added to the solution, and the precipitate was washed with large amounts of 1 M HCl solution and deionized water to obtain the H_4-PTtSAQ as a brown solid. The solid was dried under vacuum at 70 °C (9.64 g, 55% yield).

Lithiation of H_4-PTtSAQ was performed in THF using LiH as a lithiated base. In anhydrous THF (10 mL), the following was added: H_4-PTtSAQ (1.0 g, 2.15 mmol) and a stoichiometric amount of LiH (68.5 mg, 8.62 mol). The mixture was stirred at room temperature for 3 days. After that, the obtained dark precipitate was filtered and washed with diethyl ether 3 times and then transferred to a BUCHI glass oven for drying at 120 °C for 20 h to afford Li_4-PTtSAQ as a dark brown powder (1.03 g, 95% yield).

Acknowledgements

This work is funded by the Advanced Research Projects Agency-Energy (ARPA-E), US Department of Energy, under award number DE-AR0001548. The authors wish to thank Leo Jiang for TG measurements.

Conflict of Interest

Y.Y. has an equity interest in LiBeyond, LLC and Solid Design Instruments, LLC. The University of Houston reviewed and approved his relationship in compliance with its conflict-of-interest policy. The remaining authors declare no competing interests.

Author Contributions

Alae Eddine Lakraychi: conceptualization, investigation, writing, original draft. **Ifeanyi Emmanuel Udom**: complementary experiments (supporting). **Wen Ren**: complementary experiments and DFT calculation (supporting). **Yan Yao**: funding acquisition, supervision. All the authors contribute to reviewing and editing the manuscript.

Data Availability Statement

The data that support the findings of this study are available from the corresponding author upon reasonable request.

Keywords: high-voltage Li-ion organic cathodes · localized high-concentration electrolytes · multielectron small-molecule organic cathodes · solute–electrolyte interactions

[1] M. Armand, J. M. Tarascon, *Nature* **2008**, *451*, 652.
[2] A. Manthiram, *ACS Cent. Sci.* **2017**, *3*, 1063.
[3] R. Irle, *EV Sales for 2023 – Final Results*, https://ev-volumes.com/news/ev/global-ev-sales-for-2023/ (Accessed: December 2023).
[4] E. A. Olivetti, G. Ceder, G. G. Gaustad, X. Fu, *Joule* **2017**, *1*, 229.
[5] J. Baars, T. Domenech, R. Bleischwitz, H. E. Melin, O. Heidrich, *Nat. Sustainability* **2021**, *4*, 71.
[6] BloombergNEF, Battery Pack Prices Fall to an Average of $132/kWh, But Rising Commodity Prices Start To Bite, https://about.bnef.com/blog/battery-pack-prices-fall-to-an-average-of-132-kwh-but-rising-commodity-prices-start-to-bite/ (Accessed: December 2023).
[7] C. A. E. Pillot, *Lithium Ion Battery Raw Materials Supply and Demand 2016–2025*, June **2017**. http://www.avicenne.com/pdf/LithiumIon%20Battery%20Raw%20Material%20Supply%20and%20Demand%202016 2025%20C.%20Pillot%20-%20M.%20Sanders%20Presentation%20at%20AABCUS%20San%20Francisco%20June%202017.pdf.
[8] A. Manthiram, Y. Fu, S.-H. Chung, C. Zu, Y.-S. Su, *Chem. Rev.* **2014**, *114*, 11751.
[9] J.-Y. Hwang, S.-T. Myung, Y.-K. Sun, *Chem. Soc. Rev.* **2017**, *46*, 3529.
[10] Y. Liang, H. Dong, D. Aurbach, Y. Yao, *Nat. Energy* **2020**, *5*, 646.
[11] A. Innocenti, H. Adenusi, S. Passerini, *InfoMat.* **2023**, *5*, e12480.
[12] P. Poizot, J. Gaubicher, S. Renault, L. Dubois, Y. Liang, Y. Yao, *Chem. Rev.* **2020**, *120*, 6490.
[13] B. Esser, F. Dolhem, M. Becuwe, P. Poizot, A. Vlad, D. Brandell, *J. Power Sources* **2021**, *482*, 228814.
[14] J. Kim, Y. Kim, J. Yoo, G. Kwon, Y. Ko, K. Kang, *Nat. Rev. Mater.* **2023**, *8*, 54.
[15] Y. Lu, Q. Zhang, F. Li, J. Chen, *Angew. Chem., Int. Ed.* **2023**, *62*, e202216047.
[16] Y. Zhang, P. Apostol, X. Guo, X. Liu, D. Rambabu, J. Wang, X. Chen, A. Vlad, *Mater. Today Chem.* **2023**, *28*, 101379.
[17] X. Guo, P. Apostol, X. Zhou, J. Wang, X. Lin, D. Rambabu, M. Du, S. Er, A. Vlad, *Energy Environ. Sci.* **2024**, *17*, 173.
[18] L. Huang, Z. Hu, M. Li, L. Luo, J. Wang, Y. Han, H. Zhan, Z. Song, *Chem. Eng. J.* **2024**, *481*, 148447.
[19] M. Yao, N. Taguchi, H. Ando, N. Takeichi, T. Kiyobayashi, *Commun. Mater.* **2020**, *1*, 70.
[20] M. E. Speer, M. Kolek, J. J. Jassoy, J. Heine, M. Winter, P. M. Bieker, B. Esser, *Chem. Commun.* **2015**, *51*, 15261.
[21] Q. Zhao, Z. Zhu, J. Chen, *Adv. Mater.* **2017**, *29*, 1607007.
[22] A. Jouhara, N. Dupré, A.-C. Gaillot, D. Guyomard, F. Dolhem, P. Poizot, *Nat. Commun.* **2018**, *9*, 4401.
[23] A. E. Lakraychi, E. Deunf, K. Fahsi, P. Jimenez, J. P. Bonnet, F. Djedaini-Pilard, M. Bécuwe, P. Poizot, F. Dolhem, *J. Mater. Chem. A* **2018**, *6*, 19182.
[24] L. Sieuw, A. E. Lakraychi, D. Rambabu, K. Robeyns, A. Jouhara, G. Borodi, C. Morari, P. Poizot, A. Vlad, *Chem. Mater.* **2020**, *32*, 9996.
[25] J. Wang, A. E. Lakraychi, X. Liu, L. Sieuw, C. Morari, P. Poizot, A. Vlad, *Nat. Mater.* **2021**, *20*, 665.
[26] L. Bernard, A. Jouhara, E. Quarez, Y. Levieux-Souid, S. Le Caër, P. Tran-Van, S. Renault, P. Poizot, *Inorganics* **2022**, *10*, 62.
[27] W. Deng, W. Shi, P. Li, N. Hu, S. Wang, J. Wang, L. Liu, Z. Shi, J. Lin, C. Guo, *Energy Storage Mater.* **2022**, *46*, 535.
[28] J. Wang, P. Apostol, D. Rambabu, X. Guo, X. Liu, K. Robeyns, M. Du, Y. Zhang, S. Pal, R. Markowski, F. Lucaccioni, A. E. Lakraychi, C. Morari, J.-F. Gohy, D. Gupta, A. Vlad, *Sci. Adv.* **2023**, *9*, eadg6079.
[29] J. Wang, X. Guo, P. Apostol, X. Liu, K. Robeyns, L. Gence, C. Morari, J.-F. Gohy, A. Vlad, *Energy Environ. Sci.* **2022**, *15*, 3923.
[30] K. Zaghib, A. Mauger, F. Gendron, C. M. Julien, J. B. Goodenough, in *Secondary Batteries – Lithium Rechargeable Systems – Lithium-Ion | Positive Electrode: Lithium Iron Phosphate* (Ed: J. Garche), Elsevier, Amsterdam **2009**, pp. 264–296.
[31] Y. Lu, H. Han, Z. Yang, Y. Ni, Z. Meng, Q. Zhang, H. Wu, W. Xie, Z. Yan, J. Chen, *Natl. Sci. Rev.* **2024**, *11*, nwae146.
[32] A.-L. Barrès, J. Geng, G. Bonnard, S. Renault, S. Gottis, O. Mentré, C. Frayret, F. Dolhem, P. Poizot, *Chem. - Eur. J.* **2012**, *18*, 8800.
[33] S. Renault, S. Gottis, A.-L. Barrès, M. Courty, O. Chauvet, F. Dolhem, P. Poizot, *Energy Environ. Sci.* **2013**, *6*, 2124.
[34] W. Zuo, Z. Xiao, M. Zarrabeitia, X. Xue, Y. Yang, S. Passerini, *ACS Mater. Lett.* **2022**, *4*, 1074.
[35] Y. Huang, Y.-C. Lin, D. M. Jenkins, N. A. Chernova, Y. Chung, B. Radhakrishnan, I.-H. Chu, J. Fang, Q. Wang, F. Omenya, S. P. Ong, M. S. Whittingham, *ACS Appl. Mater. Interfaces* **2016**, *8*, 7013.
[36] S. Renault, D. Brandell, K. Edström, *ChemSusChem* **2014**, *7*, 2859.
[37] M. Zhao, B.-Q. Li, H.-J. Peng, H. Yuan, J.-Y. Wei, J.-Q. Huang, *Angew. Chem., Int. Ed.* **2020**, *59*, 12636.
[38] X. Gao, Z. Yu, J. Wang, X. Zheng, Y. Ye, H. Gong, X. Xiao, Y. Yang, Y. Chen, S. E. Bone, L. C. Greenburg, P. Zhang, H. Su, J. Affeld, Z. Bao, Y. Cui, *Proc. Natl. Acad. Sci.* **2023**, *120*, e2301260120.
[39] S. C. Kim, X. Gao, S.-L. Liao, H. Su, Y. Chen, W. Zhang, L. C. Greenburg, J.-A. Pan, X. Zheng, Y. Ye, M. S. Kim, P. Sayavong, A. Brest, J. Qin, Z. Bao, Y. Cui, *Nat. Commun.* **2024**, *15*, 1268.

[40] Y. Tateyama, A. Kagatsume, M. Yao, S. Matsuda, K. Uosaki, *J. Phys. Chem. C* **2023**, *127*, 12867.
[41] X. Peng, J. Guo, D. Huang, B. Ouyang, Y. Du, H. Yang, *ChemSusChem* **2024**, e202401975.
[42] Y. Liang, P. Zhang, J. Chen, *Chem. Sci.* **2013**, *4*, 1330.
[43] T. Chen, H. Banda, J. Wang, J. J. Oppenheim, A. Franceschi, M. Dincă, *ACS Cent. Sci.* **2024**, *10*, 569.
[44] Y. Lu, Z. Yang, Q. Zhang, W. Xie, J. Chen, *J. Am. Chem. Soc.* **2024**, *146*, 1100.
[45] H. Dong, O. Tutusaus, Y. Liang, Y. Zhang, Z. Lebens-Higgins, W. Yang, R. Mohtadi, Y. Yao, *Nat. Energy* **2020**, *5*, 1043.
[46] M. J. Frisch, G. W. Trucks, H. B. Schlegel, G. E. Scuseria, M. A. Robb, J. R. Cheeseman, G. Scalmani, V. Barone, G. A. Petersson, H. Nakatsuji, X. Li, M. Caricato, A. V. Marenich, J. Bloino, B. G. Janesko, R. Gomperts, B. Mennucci, H. P. Hratchian, J. V. Ortiz, A. F. Izmaylov, J. L. Sonnenberg, D. Williams-Young, F. Ding, F. Lipparini, F. Egidi, J. Goings, B. Peng, A. Petrone, T. Henderson, D. Ranasinghe, V. G. Zakrzewski, J. Gao, et al., Gaussian, Inc., Wallingford CT **2016**.
[47] T. Chen, H. Banda, L. Yang, J. Li, Y. Zhang, R. Parenti, M. Dincă, *Joule* **2023**, *7*, 986.

Manuscript received: December 31, 2024
Revised manuscript received: March 24, 2025
Version of record online: